RSC Advances

PAPER

View Article Online
View Journal | View Issue

Cite this: *RSC Adv.*, 2021, **11**, 8073

Enhancing the efficiency of the hydrogen evolution reaction utilising Fe_3P bulk modified screen-printed electrodes *via* the application of a magnetic field†

Jack. P. Hughes,[ab] Samuel Rowley-Neale *[ab] and Craig Banks *[ab]

Received 1st December 2020
Accepted 8th February 2021

DOI: 10.1039/d0ra10150h

rsc.li/rsc-advances

We report the fabrication and optimisation of Fe_3P bulk modified screen-printed electrochemical platforms (SPEs) for the hydrogen evolution reaction (HER) within acidic media. We optimise the achievable current density towards the HER of the Fe_3P SPEs by utilising ball-milled Fe_3P variants and increasing the mass percentage of Fe_3P incorporated into the SPEs. Additionally, the synergy of the application of a variable weak (constant) external magnetic field (330 mT to 40 mT) beneficially augments the current density output by 56%. This paper not only highlights the benefits of physical catalyst optimisation but also demonstrates a methodology to further enhance the cathodic efficiency of the HER with the facile application of a weak (constant) magnetic field.

Introduction

Electricity produced from renewable sources such as wind turbines, solar PV and tidal power can be converted to chemical energy in the form of green hydrogen gas.[1,2] The energy density of green hydrogen gas (140 MJ kg^{-1}) is greater than fossil fuels such as: coal (24 MJ kg^{-1}), natural gas (55 MJ kg^{-1}) and petrol (44 MJ kg^{-1}) making it a promising alternative energy source.[3] Green hydrogen is generated within an electrolyser and has no direct carbon by-products, whereas 'grey' hydrogen is produced in processes such as natural gas reformation and coal or biomass gasification where the by-products are CO_2 and CO.[4,5] The cathodic reaction within a proton exchange membrane (PEM) electrolyser is the hydrogen evolution reaction (HER; $2H^+ + 2e^- \rightarrow H_2$), where protons are electrochemically reduced to hydrogen gas formed at the surface of a suitable cathode.[6,7]

Platinum (Pt) based cathodic materials are commonly required within commercial electrolysers to carry out efficient water splitting, given that they are highly active and stable catalysts for electrolytic applications.[8] However, the application of Pt based materials within electrolysers is limited by their high cost and low abundance,[9–11] therefore research is directed towards discovering active and stable non-precious metals (NPM) cathodic catalysts.[12–15] Transition metal phosphides (TMPs) are regarded as promising cathodic catalysts, composed of active transition metals such as Ni,[16–18] Co[19–21] and Fe[22–24] which are stabilized when alloyed with phosphides.[16] An interesting study by Schipper *et al.*[25] reported on the effects of phase transition of FeP, Fe_2P and Fe_3P films electrodeposited on the surface of fluorine doped tin oxide (FTO). An increase in ferric content within the phases led to increased activity towards the HER, resulting in low HER overpotentials of 116, 83, 49 and 8 mV (*vs.* RHE) for FeP, Fe_2P, Fe_3P and Pt, respectively. The films exhibited high achievable current densities, in excess of −100 mA cm^{-2} and promising stability within acidic conditions during chronoamperometric measurements at −120 mV (*vs.* RHE) for 20 hours. Iron phosphides contain exposed stepped surfaces of 3-fold Fe and Fe–Fe bridge sites that are thought to exhibit affinity for H^+ ions.[26] FeP is mainly composed of Fe–P sites (which result in weak adsorption), where up to six P atoms are covalently bonded to an Fe^{III} centre in an orthorhombic crystal system.[27] Fe_2P consists of a combination of tetrahedral Fe^I and pyramidal Fe^{II} sites, each site arranged in a hexagonal crystal system where there are a maximum of four Fe–P interactions per Fe atom.[28,29] Within the iron phosphides, Fe_3P contains the weakest covalent bonds, but the strongest ionic interactions, metallicity and contains the largest number of Fe–Fe interactions.[30] This is a result of Fe_3P consisting of Fe^I centres arranged in a tetragonal crystal system where the increase in ferric content leads to a maximum of three Fe–P covalent bonds and an increase in favourable Fe–Fe interactions.[31] Clearly, Fe_3P is a very interesting material to study towards the HER.

In addition to material optimisation, as reported above for iron phosphides, another interesting approach to increase the cathodic efficiency of electrolysis is by using an external magnetic field.[32,33] This is due to Lorentz force induced convection *via* magnetohydrodynamic (MHD) and micro-MHD

[a]*Faculty of Science and Engineering, Manchester Metropolitan University, Chester Street, Manchester M1 5GD, UK. E-mail: c.banks@mmu.ac.uk; Fax: +44 (0) 1612476831; Tel: +44 (0)1612471196*

[b]*Manchester Fuel Cell Innovation Centre, Manchester Metropolitan University, Chester Street, Manchester M1 5GD, UK. E-mail: S.Rowley-Neale@mmu.ac.uk*

† Electronic supplementary information (ESI) available. See DOI: 10.1039/d0ra10150h

effects,[34] in which the former results in diffusion layer thinning, improving the mass and charge transfer of H^+ and e^- ions. In the latter, a perpendicular magnetic field can induce flow patterns at very small scales, close to the electrode surface (*i.e.* within the diffusion layer), which is impossible through mechanical agitation and regulates bubble removal at the electrode surface in the clockwise or anticlockwise direction, leading to the reduction of ohmic loss, and the increased availability of active sites.[34–37] Elias *et al.*[32] have studied the effect of a magnetic field on the HER by applying magnetic flux densities (B) between 0.1–0.4 T to enhance HER efficiency in Ni–W alloy electrodes. It was found that the HER onset potential of −1.35 V (*vs.* SCE) for the Ni–W electrode when $B = 0$, was reduced to −1.01 V (*vs.* SCE) when $B = 0.4$ T. Additionally, there was an increase in current density from −0.70 to *ca.* −0.82 A cm^{-2} at $B = 0.1$ T and $B = 0.4$ T, respectively. Ferromagnetic materials such as Fe, Ni and Co[38] are highly affected by an applied magnetic field and amplify the Lorentz effect, whereas materials such as Pt (paramagnetic) and graphite (diamagnetic) are largely unaffected.[39] This is due to the Zeeman effect where the distortion of electron orbitals within magnetic materials in the presence of a magnetic field leads to decreased energy barriers and enhanced electron transfer.[40] Fe_3P is a robust ferromagnetic material, hence exhibits magnetic properties that are required to enhance HER efficiency within water electrolysis.[41]

The assessment criteria of a NPM cathodic catalysts' suitability for use in PEM electrolysis is dependent upon a number of critical factors; proficient HER catalysis, high achievable current density and stability in acidic media. Another important factor, often forgotten, is the ability to translate research outputs to industry – mass-printable screen-printed electrodes can help this transition. Consequently, in this paper, we report the incorporation of Fe_3P variants into SPEs and optimise their performance as HER catalysis in acidic conditions; the effect of applying a weak magnetic field is also explored and found to provide beneficial outputs to the HER.

Experimental section

Chemicals

All chemicals used were of analytical grade from Sigma Aldrich and were without need of any further purification. The Fe_3P powder (product code: 691593; Sigma Aldrich, UK) and Fe_2P powder (product code: 691658; Sigma Aldrich, UK) utilised were of 99.5% purity (trace metals basis, −40 mesh avg. part. size). These are referred to in the text with a subscript "raw" to indicate that they were used, raw, without any treatment.

The Fe_3P powder was wet ball milled in a Retsch PM 100 planetary ball mill over the following time intervals: 5, 10, 20 and 50 h in a 50 mL zirconium oxide (ZrO_2) grinding jar (Retsch, Germany). Ball milling was carried out with 2 mm yttrium stabilized zirconia beads (Retsch, Germany) at 150 rpm, where 2 g Fe_3P was placed in 30 mL methanol to form a milling slurry. The 2 mm diameter of the zirconia beads and milling speed have been previously shown to result in the finest powder dispersion.[42] Electrochemical measurements were performed in 0.5 M H_2SO_4, which was of the highest possible purity from Sigma Aldrich (99.999%, double distilled for trace metal analysis).

Electrochemical measurements

The electrolyte (0.5 M H_2SO_4) was made using deionized water (resistivity 18.2 MΩ cm), which was degassed with high purity nitrogen before electrochemical measurements. It is common within research conducting HER experiments to remove any trace of oxygen, to prevent the onset of the competing ORR. An Autolab Compact™ (Switzerland) potentiostat was used to carry out electrochemical measurements. A three-electrode system was used to take measurements with modified and bare graphitic screen printed electrodes (SPEs) with a working area diameter of 3.1 mm used as working electrodes, with a carbon counter and a saturated calomel electrode (SCE) reference. The neodymium ring magnets (30 × 10 × 10 I.D. mm, magnetic field strength: 0.44 T, First4Magnets, product code: F3010DM-1) used for electrochemical measurements were placed in incremental distances from the electrode surface, highlighted in the ESI Table T1.† The screen-printing process used to produce the Fe_2P and Fe_3P SPEs utilised within this study is explained within the ESI† and is also described in more depth in previous studies.[11,43–45] Herein, the potential is referenced to the reversible hydrogen electrode (RHE) utilising the following equation, as is common within the literature:[46–48] $E_{RHE} = E_{SCE} + 0.059pH + 0.242$ V (at 25 °C).

Physicochemical characterisation of the raw and ball milled Fe_3P powders

It was important to assess the particle size and distribution of the raw Fe_3P powder using Scanning Electron Microscopy (SEM) and Energy Dispersive X-ray (EDX) elemental mapping to compare against the (wet) ball-milled variants. In the ESI, Fig. S1(A_1)† shows an SEM image of the raw Fe_3P powder, where the average particle size is *ca.* 400 μm. SEM images in Fig. S1(A_{2-5})† depict the reduction in particle size of the ball milled Fe_3P powders. The average particle size of the 5, 10 and 20 h ball-milled Fe_3P powders is >10 μm, whereas the Fe_3P powder ball milled for 50 h is <1 μm. After 20 h of ball milling, a cold welding process has likely occurred and the Fe_3P particles have aggregated changing the microscopic structure from crystalline to amorphous, which is also shown in the EDX elemental mapping images in Fig. S1(B_{1-5})†. The corresponding EDX elemental analysis is exhibited in ESI Table T2,† showing elemental compositions of carbon, oxygen, iron and phosphorous. The initial ratio of Fe : P is shown to be 8 : 1, which could be a result of the non-uniform distribution due to the (relatively) large average particle size. The Fe : P ratio is steadily reduced as the ball-milling duration increases, where a ratio of 5 : 1 is observed at 50 h. The percentage composition of oxygen within the Fe_3P powders increases with ball milling duration, where raw Fe_3P contains 3.5% and 50 h ball milled Fe_3P contains 11.5% oxygen. It is expected that ball-milling in an air atmosphere, as employed here, will lead to an increase in oxygen concentration and the ball milled Fe_3P powders will likely be

covered with a thin oxide layer. The thin oxide layer is thought to make the powder particles brittle, therefore resulting in a finer dispersion when the amorphous powder is agitated.[49] The presence of carbon within the raw and ball milled Fe_3P powders is a result of the wet milling process in the presence of methanol.

X-ray Diffraction (XRD) analysis can be used more accurately to assess the crystallinity of the raw and ball milled Fe_3P powders. Fig. S2(A)† exhibits the characteristic diffraction peaks of raw Fe_3P at $2\theta = 35.9°$, 40.5°, 41.2°, 42.2°, 43.1°, 44.6°, 45.4°, 46.0°, 47.5°, 49.9°, 51.3°, 52.0°, 53.1° and 54.5°, which are indexed towards the following single crystal faces of Fe_3P, respectively; (301), (321), (330), (112), (420), (141), (400), (222), (110), (530), (620), (541), (422) and (212).[50,51] Fig. S2(B–E)† exhibit XRD spectra of the ball milled variants of Fe_3P powder in the time intervals 5, 10, 20 and 50 h, respectively. The spectra become increasingly convoluted, hence show a reduction in the crystallinity of Fe_3P as the ball-milling time increases. The following single crystal faces within the milled powders are detected; (301), (330), (420), (141), (222), (530), (541) and (212). This suggests a transformation from crystalline to amorphous, as observed above.

Raman Spectroscopy was used to further characterise the raw and ball milled Fe_3P powders. Fig. S3(A)† shows the Raman spectrum for raw Fe_3P, exhibiting characteristic vibrational bands at *ca.* 655 and 1339 cm^{-1}, which correspond to the Fe–O (A_g1) symmetric stretching mode and first order carbon (D) band.[52] The Fe–O and carbon vibrational bands are likely present as a result of the methanol milling within the presence of air. The Raman spectra of the 5, 10, 20 and 50 h ball milled Fe_3P powders are shown in Fig. S3(B)–(E)†, respectively. Additional characteristic vibrational bands are present within the spectra for each of the milled Fe_3P variants at *ca.* 214, 391 and 488 cm^{-1} corresponding to Fe–O symmetric stretching modes. Vibrational bands at 291 and 523 cm^{-1} within the milled Fe_3P samples indicate Fe–O asymmetric bending modes (T_g2).[52]

X-ray Photoelectron Spectroscopy (XPS) was used to assess the surface elemental composition of the raw and ball milled Fe_3P powders. The XPS profiles of Fe $2p_{3/2}$, Fe $2p_{1/2}$ and P 2p shown in Fig. S4† are consistent with the findings in literature.[53–55] The Fe spectra in Fig.S4(A_{1-5})† correspond to Fe^{3+} as they exhibit well-defined satellite peaks that are approximately 8 eV from the centre of the main Fe $2p_{3/2}$ peak at 710 eV. The Fe $2p_{1/2}$ bands at *ca.* 720 and 725 eV correspond to Fe^{2+} (Fe–O) and Fe^{3+} (Fe–P), respectively.[56] The P 2p spectra in Fig. S4(B_{1-5})† exhibit peaks at 128.6 and 129.9 eV, which correspond to $2p_{3/2}$ and $2p_{1/2}$, respectively, where the peak at 129.9 eV is a result of Fe–P bonding within Fe_3P.[54] The peak at 133.0 eV corresponds to P^{5+}, indicating P–O bonding in $FePO_4$, which is also suggested in the Fe 2p spectra through the presence of Fe^{3+}.[57,58] The XPS findings are consistent with the Raman spectroscopy, where partial surface oxidation is suggested. The above physicochemical characterisation techniques have confirmed the presence of crystalline and amorphous Fe_3P within the raw and ball-milled samples.

Results and discussion

Exploring Fe_2P and Fe_3P bulk modified screen-printed electrodes (SPEs) towards the hydrogen evolution reaction (HER)

The HER activity of Fe_2P and Fe_3P bulk modified SPEs, fabricated as described in detail in the Experimental section, were first evaluated within acid media (0.5 M H_2SO_4). Fig. 1(A) shows linear sweep voltammetry (LSV) obtained for the different % Fe_2P SPE_{Raw} variants (5, 10, 20 and 40%), which have been benchmarked against a bare SPE (no Fe_2P) and a polycrystalline Pt electrode. Note that the subscript "Raw" is given to these, as the untreated raw powder, is utilised. The polycrystalline Pt electrode, as expected, exhibits optimal HER activity with an onset of −0.01 V (*vs.* RHE). HER onset potential values of −0.53, −0.21, −0.20, −0.19 and −0.17 V (*vs.* RHE) are exhibited by the bare SPE, 5% Fe_2P SPE_{Raw}, 10% Fe_2P SPE_{Raw}, 20% Fe_2P SPE_{Raw} and 40% Fe_2P SPE_{Raw}, respectively (NB: the HER onset potential is defined as the point at which the observed current deviates from the background current by −25 μA cm^{-2}).[59] The most electronegative HER onset potential is displayed by the bare SPE, where the graphitic carbon layer is solely responsible for the observed HER catalysis; this response is as expected and observed previously. The closest HER onset potential to the Pt electrode is obtained using the 40% Fe_2P SPE_{Raw}, which possesses the highest loading of the Fe_2P catalyst, therefore the highest number of electroactive sites. The polycrystalline Pt electrode also exhibits the optimal achievable current density, requiring −0.06 V (*vs.* RHE) to reach −10 mA cm^{-2}. None of the Fe_2P SPEs reached the −10 mA cm^{-2} current density standard, marked as a dashed line in Fig. 1.

Fig. 1(B) also shows LSV obtained for the 5% Fe_3P SPE_{Raw}, 10% Fe_3P SPE_{Raw}, 20% Fe_3P SPE_{Raw} and 40% Fe_3P SPE_{Raw}, again, benchmarked against a bare SPE and a polycrystalline Pt electrode. HER onset potential values of −0.53, −0.14, −0.13, −0.11 and −0.11 V (*vs.* RHE) were exhibited by the bare SPE, 5% Fe_3P SPE_{Raw}, 10% Fe_3P SPE_{Raw}, 20% Fe_3P SPE_{Raw} and 40% Fe_3P SPE_{Raw}, respectively. The least electronegative HER onset potential was exhibited by the 20 and 40% Fe_3P SPE_{Raw} due to the higher loading of Fe_3P catalyst within SPEs. A higher achievable current density is observed within the Fe_3P SPEs compared to the Fe_2P SPEs, where the 20% Fe_3P SPE_{Raw} and 40% Fe_3P SPE_{Raw} required −1.13 and −1.24 V (*vs.* RHE) to reach −10 mA cm^{-2}. This is likely due to the increase in ferric content, where a greater number of Fe–Fe bridge sites result in a faster heterogeneous electron transfer (HET) rate.[25] It is evident that a 20% incorporation of Fe_3P within SPEs is the optimal mass loading with no significant improvement with 40%, and in fact, is worse than the 20% incorporation, which is likely due to partial blockage of active sites at the electrode surface and reduced conductive electronic pathways within the graphite electrode.[6,11,43] Note that further loadings of the Fe_3P result in difficulties in screen-printing due to the change in rheology and represents the limit; this has seen multiple times for materials incorporated into bulk SPEs by our group. Given that the 20% Fe_3P SPE_{Raw} is the nearest in HER activity to the optimal Pt

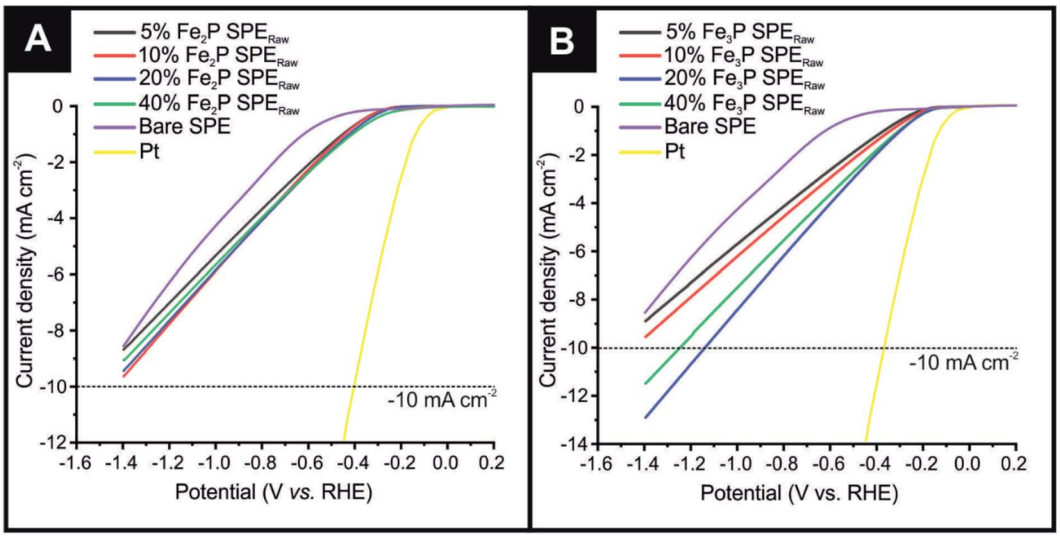

Fig. 1 (A) Linear sweep voltammetry (LSV) exhibiting the onset potential of the HER, in the potential range +0.2 to −1.4 V (*vs.* RHE) for the Fe_2P SPEs produced from raw powder: Fe_2P $SPE_{5\%}$, Fe_2P $SPE_{10\%}$, Fe_2P $SPE_{20\%}$, Fe_2P $SPE_{40\%}$, bare/unmodified SPE and polycrystalline Pt. (B) And for the Fe_3P SPEs produced from raw powder: Fe_3P $SPE_{5\%}$, Fe_3P $SPE_{10\%}$, Fe_3P $SPE_{20\%}$, Fe_3P $SPE_{40\%}$ bare/unmodified SPE and polycrystalline Pt. Scan rate: 25 mV s^{-1} (*vs.* RHE) in 0.5 M H_2SO_4.

electrode, this mass loading of Fe_3P only was taken forward for further exploration towards the HER.

Next, ball-milling was utilised to try and tune/improve the HER kinetics of the Fe_3P further, which is facilitated by reducing the average particle size and increasing porosity; such an approach has been previously reported for other materials.[60–62] Consequently, raw Fe_3P powder was ball milled over various time intervals (5, 10, 20 and 50 h) and the resultant powders incorporated into the bulk of bespoke SPEs and benchmarked against the HER within acidic media. Note that a full physicochemical characterization was performed on the raw and ball milled Fe_3P powders utilized, as it is the focus of HER exploration within this paper (see Experimental section and ESI†), but not performed on the Fe_2P powders.

Fig. 2 shows LSVs obtained for the Fe_3P $SPE_{5\ h}$, Fe_3P $SPE_{10\ h}$, Fe_3P $SPE_{20\ h}$ and Fe_3P $SPE_{50\ h}$, benchmarked against a bare SPE and a polycrystalline Pt electrode. HER onset potential values of −0.53, −0.12, −0.11, −0.11 and −0.12 V (*vs.* RHE) are exhibited by the bare SPE, Fe_3P $SPE_{5\ h}$, Fe_3P $SPE_{10\ h}$, Fe_3P $SPE_{20\ h}$ and Fe_3P $SPE_{50\ h}$, respectively. The applied potentials of: −1.04, −0.91, −0.84 and −1.14 V (*vs.* RHE) were required to reach −10 mA cm^{-2} for the Fe_3P $SPE_{5\ h}$, Fe_3P $SPE_{10\ h}$, Fe_3P $SPE_{20\ h}$ and Fe_3P $SPE_{50\ h}$, respectively. The HER onset potentials displayed by the ball milled Fe_3P SPEs show that the HER kinetics of each SPE have remained stable as a result of increased ball milling time. The applied potential required to reach −10 mA cm^{-2} for all Fe_3P electrodes was greatly reduced with milling time, excluding the Fe_3P $SPE_{50\ h\ BM}$, which has marginally increased. It is evident that there is an optimal duration of ball milling, where a 25.7% reduction in applied potential to reach −10 mA cm^{-2} is exhibited by the Fe_3P $SPE_{20\ h\ BM}$ compared to the unmilled variant. This is due to increasing ball-milling time leading to an increase in specific surface area and a decrease in crystal size and micropore diameter of the Fe_3P powder. Note, that as the micropore diameter is reduced, porosity is increased with respect to increased micropore ratio. It is likely that the micropore diameter (nm) decreases up to 20 h of ball milling, then begins to plateau or increase moving towards 50 h. This is because there is an increase in the maximum distribution of nanoparticles (P_{max}) after which porosity is reduced as a result of cluster formation.[63] The Fe_3P powder ball milled for 20 h

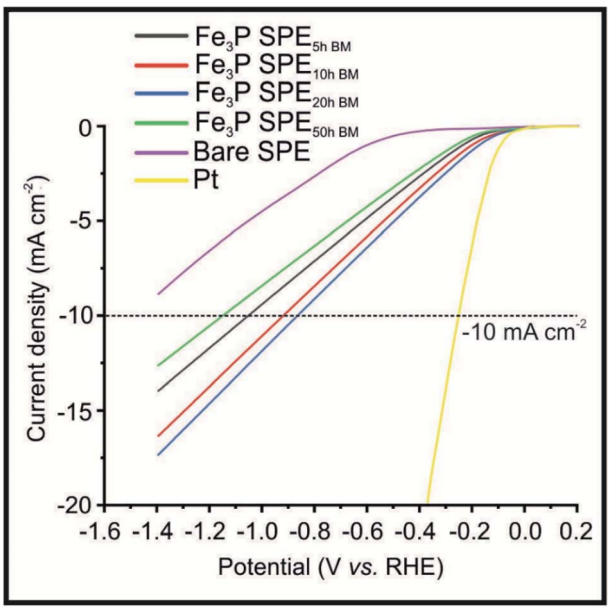

Fig. 2 Linear sweep voltammetry (LSV) exhibiting the onset potential of the HER, in the potential range +0.2 to −1.4 V (*vs.* RHE) for the 20% Fe_3P SPEs produced from ball milled (BM) powder: Fe_3P $SPE_{5\ h\ BM}$, Fe_3P $SPE_{10\ h\ BM}$, Fe_3P $SPE_{20\ h\ BM}$, Fe_3P $SPE_{50\ h\ BM}$, bare/unmodified SPE and polycrystalline Pt. Scan rate: 25 mV s^{-1} (*vs.* RHE) in 0.5 M H_2SO_4.

possesses the greatest porosity and therefore the higher ratio of Fe–Fe bridge sites to Fe–P sites. The Fe_3P $SPE_{5\ h}$, Fe_3P $SPE_{10\ h}$, Fe_3P $SPE_{20\ h}$ and Fe_3P $SPE_{50\ h}$ exhibit specific activities of 0.296, 0.297, 0.314 and 0.306 A cm^{-2}, respectively, hence displaying the optimal ball milling time of 20 h. Tafel analysis was used in a qualitative manner, in order assess whether there was an alteration in the HER reaction mechanism as the ball milling time increased. Tafel analysis extrapolated from the faradaic regions of the LSV's presented in Fig. 2 with values of 118.1, 88.5, 101.4, 95.6 and 96.4 mV dec^{-1} are exhibited by the bare SPE, Fe_3P $SPE_{5\ h}$, Fe_3P $SPE_{10\ h}$, Fe_3P $SPE_{20\ h}$ and Fe_3P $SPE_{50\ h}$, respectively. This suggests that there is no change in the rate limiting HER step, which closely matches that expected for the Volmer step/mechanism. Last, the current literature has been surveyed with respect to transition metal phosphides (TMPs), as shown in the ESI (ESI Table T3†) where all other approaches have utilised drop-casting. It is evident that the our Fe_3P bulk modified SPEs perform comparably with previous TMPs with our approach potentially offering a greater transition from academia to industry based upon that fact that these Fe_3P SPEs can offer mass production and scales of economy.

Electrochemical performance of the Fe_3P SPEs towards the HER under a weak (constant) magnetic field

The optimised Fe_3P SPEs were next explored towards the HER under the effect of a weak (constant) magnetic field applied perpendicular ($B-$). As shown in Fig. 3, the 20% Fe_3P SPE_{Raw} displayed the following potential values to reach -10 mA cm^{-2} of -1.13, -1.07, -1.09, -1.11 and -1.13 (*vs.* RHE) which correspond to the *B* values of: 0 (magnet off), 0.29, 0.33, 0.15 and 0.04 T, respectively. The potential values for the 20% Fe_3P $SPE_{20\ h\ BM}$ to reach -10 mA cm^{-2} of -0.84, -0.77, -0.74, -0.82 and -0.84 V (*vs.* RHE) correspond to the *B* values listed above. It is evident that applying a larger magnetic flux density beneficially alters the HER catalysis exhibited by the 20% Fe_3P SPE_{Raw} where a 56% improvement, compared to the bare SPE, is observed at the maximum flux density (*B*).

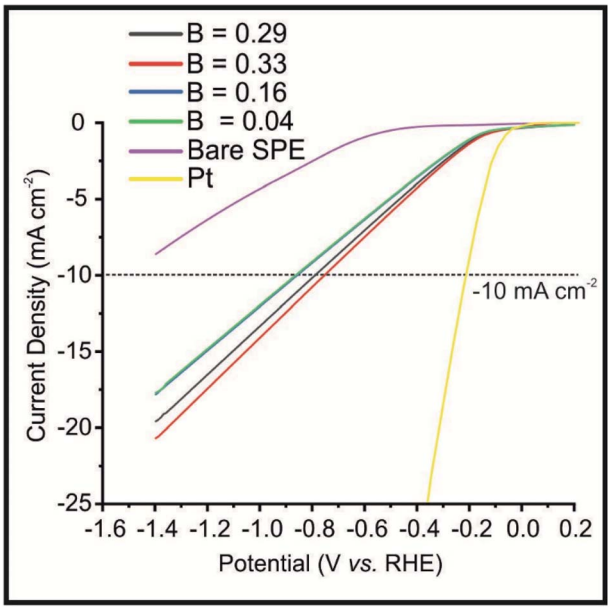

Fig. 3 Linear sweep voltammetry (LSV) exhibiting the onset potential of the HER under an applied magnetic field, in the potential range +0.2 to -1.4 V (*vs.* RHE) for the Fe_3P $SPE_{20\ h\ BM}$ at the following magnetic flux densities: 0.29, 0.33, 0.16 and 0.04 T. Scan rate: 25 mV s^{-1} (*vs.* RHE) in 0.5 M H_2SO_4.

The increase in HER activity can be visually observed, *via* being held at a potential of -0.50 (*vs.* RHE) in the ESI (see Video S1†), using the Fe_3P $SPE_{20\ h\ BM}$. It is evident that hydrogen bubbles are produced at a faster rate upon the surface of the Fe_3P $SPE_{20\ BM}$, as the magnetic flux density is increased, when the magnet is brought closer to the electrode surface. A suitable way to demonstrate this increased rate of hydrogen gas output is calculating the hydrogen turnover frequency (ToF) with and without the effect of magnetic field. ToF calculations, shown in the ESI,† for the Fe_3P $SPE_{20\ h}$ with and without a magnetic field, exhibit values of 2.72×10^{-7}, 5.61×10^{-7}, 5.67×10^{-7}, 4.17×10^{-7} and 3.30×10^{-7} H_2 per s per active site, corresponding to the following values of *B*: 0, 0.29, 0.33, 0.15 and 0.04 T respectively; this suggests that applying a magnetic field enhances the kinetics of the HER.

Commercial PEM electrolysis requires the use of cathodic catalysts that exhibit long-term stability and current retention in acidic conditions. Therefore, chronoamperometry, shown in ESI (Fig. S5†), was carried out using the Fe_3P $SPE_{20\ h\ BM}$ at -0.50 V (*vs.* RHE) for a duration of 24 h in 0.5 M H_2SO_4, in the presence of a magnetic field ($B = 0.33$ T). It is clear that the Fe_3P $SPE_{20\ h\ BM}$ retains nearly 100% of its current density at 2.98 mA cm^{-2} for 24 h, in exception to a drop in current density at 15 h to *ca.* 2 mA cm^{-2} until 20 h, where the current density returns to 2.98 mA cm^{-2}.

Last, the reason for the increase of 56% and the improvement of the ToF under the application of a weak (constant) magnetic field needs to be surmised. It is important to ascertain whether the observed response (beneficial signal output with regards to a greater achievable HER curreny density) is due to the application of the magnetic field improving the electron transfer/heterogeneous rate kinetics between the electrode surface and the proton, or other factors. It is likely that the following factors contribute: (1) ferromagnetic materials, such as Fe_3P utilised here, exhibit increased electron transfer efficiency due to higher energy electrons (as a result of the external magnetic field) within the conductive graphitic substrate transferring to the Fe_3P active sites at a faster rate; (2) Fe_3P possesses greatest porosity and larger surface area, after 20 h ball milling, therefore a higher number of distributed Fe–Fe bridge active sites where high energy electrons will have an increased number of electronic pathways to active sites; (3) the application of the magnetic field may also attributed to the Lorentz force, which induces convection *via* magnetohydrodynamic [MHD] and micro-MHD effects, resulting in diffusion layer thinning and removal of hydrogen gas bubbles from the electrode surface, increasing the availability of active sites on the electrode surface and increasing the ToF. Since hydrogen gas is diamagnetic, the direct effect of the magnetic field is likely to be relatively negligible. Thus, based on the

observations herein, it is likely that the effect of the magnetic field improving the hydrogen evolution reaction is not kinetic/charge transfer in nature but rather that of mass-transport. This is a truly interesting field worthy of further insight.

Conclusions

To summarise, we have demonstrated the proficient activity of Fe_3P SPE's towards the HER in an acidic electrolyte where the Fe_3P material was incorporated into bulk modified SPEs. Ball-milling of the raw Fe_3P powder prior to incorporation into the SPEs was utilised as a means to tune the HER kinetics of the Fe_3P SPEs, by reducing average particle size. An external magnetic field was utilised to further optimise the HER activity exhibited by the ball-milled Fe_3P SPEs, where a weak magnetic flux density resulted in a beneficial increase of 56%. The Fe_3P $SPE_{20\ h\ BM}$ exhibited excellent stability over the course of a 20 h chronoamperometric measurement at −0.50 V (*vs.* RHE) under a magnetic field (0.33 T), retaining 100% of its current density. The proficient HER activity and long term stability of the ball milled Fe_3P SPEs in acidic conditions, under weak magnetic control, represents the first instance of SPEs utilised within a magnetic field, where applying a weak magnetic field reduces the requirement for costly magnetic components. This work opens up an entire field of unexplored research and demonstrates an advancement in the field of PEM electrolysis, helping transition this work closer to industrial uptake as the Fe_3P bulk modified SPEs can be mass-produced and have scales of economy.

Conflicts of interest

The authors declare no competing financial interest.

Acknowledgements

This study is funded by Innovate UK (Reference: 11607) in cooperation with the European Marine Energy Centre (EMEC). Funding is also from the Engineering and Physical Sciences Research Council (Reference: EP/P007767/1 and EP/N0011877/1). The Manchester Fuel Cell Innovation Centre is funded by the European Regional Development Fund.

References

1 S. E. Hosseini and M. A. Wahid, *Renewable Sustainable Energy Rev.*, 2016, **57**, 850–866.
2 I. Dincer and C. Acar, *Int. J. Hydrogen Energy*, 2015, **40**(34), 11094–11111.
3 World Nuclear Association, *Heat Values of Various Fuels*, https://www.world-nuclear.org/information-library/facts-and-figures/heat-values-of-various-fuels.aspx, accessed 16/01/2020.
4 F. Isorna, F. Segura and J. A. Marquez, *Green hydrogen production methods. A review of solar-driven water splitting techniques*, 2018.
5 T. R. Ayodele and J. L. Munda, *Int. J. Hydrogen Energy*, 2019, **44**(33), 17669–17687.
6 J. P. Hughes, F. D. Blanco, C. E. Banks and S. J. Rowley-Neale, *RSC Adv.*, 2019, **9**(43), 25003–25011.
7 P. S. Adarakatti, M. Mahanthappa, J. P. Hughes, S. J. Rowley-Neale, G. C. Smith, S. Ashoka and C. E. Banks, *Int. J. Hydrogen Energy*, 2019, **44**(31), 16069–16078.
8 M. Karuppannan, Y. Kim, S. Gok, E. Lee, J. Y. Hwang, J.-H. Jang, Y.-H. Cho, T. Lim, Y.-E. Sung and O. J. Kwon, *Energy Environ. Sci.*, 2019, **12**(9), 2820–2829.
9 S. J. Rowley-Neale, D. A. C. Brownson, G. C. Smith, D. A. G. Sawtell, P. Kelly and C. E. Banks, *Nanoscale*, 2015, **7**(43), 18152–18168.
10 S. Rowley-Neale, M. Ratova, L. Fugita, G. Smith, A. Gaffar, J. Kulczyk-Malecka, P. Kelly and C. Banks, *ACS Omega*, 2018, **3**(7), 7235–7242.
11 S. J. Rowley-Neale, C. W. Foster, G. C. Smith, D. A. C. Brownson and C. E. Banks, *Sustainable Energy Fuels*, 2017, **1**(1), 74–83.
12 G. Hu, J. Li, P. Liu, X. Zhu, X. W. Li, R. N. Ali and B. Xiang, *Appl. Surf. Sci.*, 2019, **463**, 275–282.
13 J. Hao, W. Yang, Z. Zhang and J. Tang, *Nanoscale*, 2015, **7**(25), 11055–11062.
14 B.-W. Ahn, T.-Y. Kim, S.-H. Kim, Y.-I. Song and S.-J. Suh, *Appl. Surf. Sci.*, 2018, **432**, 183–189.
15 A. Sumboja, T. An, H. Y. Goh, M. Lübke, D. P. Howard, Y. Xu, A. D. Handoko, Y. Zong and Z. Liu, *ACS Appl. Mater. Interfaces*, 2018, **10**(18), 15673–15680.
16 A. R. J. Kucernak and V. N. N. Sundaram, *J. Mater. Chem. A*, 2014, **2**(41), 17435–17445.
17 J.-S. Moon, J.-H. Jang, E.-G. Kim, Y.-H. Chung, S. J. Yoo and Y.-K. Lee, *J. Catal.*, 2015, **326**, 92–99.
18 B. You, N. Jiang, M. Sheng, M. W. Bhushan and Y. Sun, *ACS Catal.*, 2016, **6**(2), 714–721.
19 F. Du, Y. Zhang, H. He, T. Li, G. Wen, Y. Zhou and Z. Zou, *J. Power Sources*, 2019, **431**, 182–188.
20 Z. Zhu, Y. Yang, Y. Guan, J. Xue and L. Cui, *J. Mater. Chem. A*, 2016, **4**(40), 15536–15545.
21 Y. Li, S. Niu, D. Rakov, Y. Wang, M. Cabán-Acevedo, S. Zheng, B. Song and P. Xu, *Nanoscale*, 2018, **10**(15), 7291–7297.
22 F. Wang, X. Yang, B. Dong, X. Yu, H. Xue and L. Feng, *Electrochem. Commun.*, 2018, **92**, 33–38.
23 H. Du, S. Gu, R. Liu and C. M. Li, *Int. J. Hydrogen Energy*, 2015, **40**(41), 14272–14278.
24 Z. Gao, Q. Gao, Z. Liu, C. Zhang, X. Zhang, X. Liu, R. Wang and N. Li, *RSC Adv.*, 2016, **6**(115), 114430–114435.
25 D. E. Schipper, Z. Zhao, H. Thirumalai, A. P. Leitner, S. L. Donaldson, A. Kumar, F. Qin, Z. Wang, L. C. Grabow, J. Bao and K. H. Whitmire, *Chem. Mater.*, 2018, **30**(10), 3588–3598.
26 D. E. Schipper, Z. Zhao, H. Thirumalai, A. P. Leitner, S. L. Donaldson, A. Kumar, F. Qin, Z. Wang, L. C. Grabow, J. Bao and K. H. Whitmire, *Chem. Mater.*, 2018, **30**(10), 3588–3598.
27 K. Persson, *Materials Data on FeP (SG:62) by Materials Project*, Energy, U. S. D. o., Ed., 2015.

28 E. Kha, S. Bhat, S.-C. Lee and S. Bhattacharjee, *Cu-substituted Fe_2P: An emerging candidates for magnetic RAM application*. 2019.
29 K. Persson, *Materials Data on Fe2P (SG:189) by Materials Project*, Energy, U. S. D. o., Ed., 2016.
30 J. Wu, X. Y. Chong, R. Zhou, Y. H. Jiang and J. Feng, *RSC Adv.*, 2015, **5**(100), 81943–81956.
31 K. Persson, *Materials Data on Fe3P (SG:82) by Materials Project*, Energy, U. S. D. o., Ed., 2016.
32 L. Elias and H. A. Chitharanjan, *Electrocatalysis*, 2017, **8**(4), 375–382.
33 F. A. Garcés-Pineda, M. Blasco-Ahicart, D. Nieto-Castro, N. López and J. R. Galán-Mascarós, *Nat. Energy*, 2019, **4**(6), 519–525.
34 V. Gatard, J. Deseure and M. Chatenet, *Curr. Opin. Electrochem.*, 2020, **23**, 96–105.
35 Y. Li, L. Zhang, J. Peng, W. Zhang and K. Peng, *J. Power Sources*, 2019, **433**, 226704.
36 M. Sheikholeslami and D. D. Ganji in *External Magnetic Field Effects on Hydrothermal Treatment of Nanofluid*, ed. M. Sheikholeslami and D. D. Ganji, William Andrew Publishing, 2016, pp. 1–47.
37 N. Leventis and X. Gao, *Anal. Chem.*, 2001, **73**(16), 3981–3992.
38 M. D. Kuz'min and M. Richter in *Encyclopedia of Materials: Science and Technology*, ed. K. H. J. Buschow, R. W. Cahn, M. C. Flemings, B. Ilschner, E. J. Kramer, S. Mahajan and P. Veyssière, Elsevier, Oxford, 2007, pp. 1–7.
39 M.-Y. Lin, L.-W. Hourng and C.-W. Kuo, *Int. J. Hydrogen Energy*, 2012, **37**(2), 1311–1320.
40 Z. Zeng, T. Zhang, Y. Liu, W. Zhang, Z. Yin, Z. Ji and J. Wei, *ChemSusChem*, 2018, **11**(3), 580–588.
41 E. J. Lisher, C. Wilkinson, T. Ericsson, L. Haggstrom, L. Lundgren and R. Wappling, *J. Phys. C: Solid State Phys.*, 1974, **7**(7), 1344–1352.
42 H. Shin, S. Lee, H. S. Jung and J.-B. Kim, *Ceram. Int.*, 2013, **39**(8), 8963–8968.
43 S. J. Rowley-Neale, D. A. C. Brownson, G. C. Smith, D. A. G. Sawtell, P. J. Kelly and C. E. Banks, *Nanoscale*, 2015, **7**(43), 18152–18168.
44 S. J. Rowley-Neale, G. C. Smith and C. E. Banks, *ACS Appl. Mater. Interfaces*, 2017, **9**(27), 22539–22548.
45 A. G.-M. Ferrari, C. W. Foster, P. J. Kelly, D. A. C. Brownson and C. E. Banks, *Biosensors*, 2018, **8**(2), 53.
46 K. Li, C. Zhang, X. Li, Y. Du, P. Yang and M. Zhu, *Catal. Today*, 2018, **335**, 173–179.
47 C. Wang, W. D. Wu, Y. Wang, D. Xu and F. Yan, *New J. Chem.*, 2017, **41**(15), 7392–7399.
48 X. Wang, W. Xiao, J. Zhang, Z. Wang and X. Jin, *Electrochem. Commun.*, 2019, **102**, 52–56.
49 B. Madavali, J.-H. Lee, J. K. Lee, K. Y. Cho, S. Challapalli and S.-J. Hong, *Powder Technol.*, 2014, **256**, 251–256.
50 E. Lisher, C. Wilkinson, T. Ericsson, L. Haggstrom, L. Lundgren and R. Wappling, *J. Phys. C: Solid State Phys.*, 2001, **7**, 1344.
51 X. Lai, F. Zhu, Y. Liu, W. Bi, J. Zhao, E. E. Alp, M. Y. Hu, D. Zhang, S. Tkachev, M. H. Manghnani, V. B. Prakapenka and B. Chen, *Earth Planet. Sci. Lett.*, 2020, **531**, 115974.
52 C. Pirim, M. A. Pasek, D. A. Sokolov, A. N. Sidorov, R. D. Gann and T. M. Orlando, *Geochim. Cosmochim. Acta*, 2014, **140**, 259–274.
53 Y. Wang, L. Zhang, H. Li, Y. Wang, L. Jiao, H. Yuan, L. Chen, H. Tang and X. Yang, *J. Power Sources*, 2014, **253**, 360–365.
54 C. Y. Son, I. H. Kwak, Y. R. Lim and J. Park, *Chem. Commun.*, 2016, **52**(13), 2819–2822.
55 T. Plachy, E. Kutalkova, M. Sedlacik, A. Vesel, M. Masar and I. Kuritka, *J. Ind. Eng. Chem.*, 2018, **66**, 362–369.
56 F.-X. Ma, C.-Y. Xu, F. Lyu, B. Song, S.-C. Sun, Y. Y. Li, J. Lu and L. Zhen, *Adv. Sci.*, 2019, **6**(3), 1801490.
57 G. Cho, H. Kim, Y. S. Park, Y.-K. Hong and D.-Y. Ha, *Int. J. Hydrogen Energy*, 2018, **43**(24), 11326–11334.
58 S. Yao, V. Forstner, P. W. Menezes, C. Panda, S. Mebs, E. M. Zolnhofer, M. E. Miehlich, T. Szilvási, N. A. Kumar, M. Haumann, K. Meyer, H. Grützmacher and M. Driess, *Chem. Sci.*, 2018, **9**(45), 8590–8597.
59 J. Scremin, I. V. J. d. Santos, J. P. Hughes, A. G.-M. Ferrari, E. Valderrama, W. Zheng, X. Zhong, X. Zhao, E. J. R. Sartori, R. D. Crapnell, S. J. Rowley-Neale and C. E. Banks, *Nanoscale*, 2020, (12), 18214–18224.
60 M. Ma, K. Chen, J. Jiang, X. Yang, H. Wang, H. Shao, J. Liu and L. Ouyang, *Inorg. Chem. Front.*, 2020, **7**(4), 918–929.
61 L.-F. Zhang, X. Ke, G. Ou, H. Wei, L.-N. Wang and H. Wu, *Sci. China Mater.*, 2017, **60**(9), 849–856.
62 X. Liu, Y. Guo, W. Zhan and T. Jin, *Catalysts*, 2019, **9**, 240.
63 T. T. Bui, X. Q. Le, D. P. To and V. T. Nguyen, *Adv. Nat. Sci.: Nanosci. Nanotechnol.*, 2013, **4**(4), 045003.